

Bubble Behavior and Size Distributions in Stopper-Rod Nozzle and Mold during Continuous Casting of Steel Slabs

Seong-Mook CHO,¹⁾ Brian G. THOMAS^{1,2)*} and Seon-Hyo KIM³⁾

1) Department of Mechanical Engineering, Colorado School of Mines, 1610 Illinois Street, Golden, Colorado, 80401 USA.
 2) Department of Mechanical Science and Engineering, University of Illinois at Urbana-Champaign, 1206 West Green Street, Urbana, Illinois, 61801 USA. 3) Department of Materials Science & Engineering, Pohang University of Science & Technology, 77 Cheongam-Ro, Nam-Gu, Pohang, Gyeongbuk, 790-784 Republic of Korea.

(Received on February 9, 2018; accepted on May 14, 2018)

Argon-gas injection parameters including flow rate and bubble size distribution are important to prevent nozzle clogging, control the mold flow, and reduce bubble-related defects in steel continuous casting. This work employs water-air model experiments and analytical modeling to quantify the behavior and size distributions of gas bubbles in the nozzle and mold during nominally steady-state slab-casting, focusing on gas injection through a stopper-rod with multiple side-channels. Bubble formation, breakup, coalescence, and accumulation are investigated with experiments using a one-third scale water model with the aid of high-speed video recording and analytical models to predict gas pressure, initial bubble size, bubble descending velocity, bubble residence time, and bubble size distribution considering accumulation. In addition, size distributions of the bubbles in the nozzle and mold are quantified by analyzing snapshots of bubble images. Bubbles initiate at the gas channel exit in the stopper-rod after overcoming the pressure threshold, and then expand and elongate until detaching from the stopper-rod surface. After that, turbulent flow breaks up the bubbles inside the gap between the stopper-rod and the nozzle inlet. The bubbles sometimes coalesce with others, and get bigger while flowing down through the nozzle. The bigger bubbles have longer residence time, and accumulate in the nozzle, due to higher buoyancy on them. With higher gas flow-rate, bubble size distribution in the nozzle and mold shows larger average-size and broader size-range. Finally, the validated initial bubble-size model with the water-air model measurements is extrapolated to estimate argon-bubble sizes in molten steel with real caster conditions.

KEY WORDS: multiphase flow; argon; bubble; breakup; coalescence; accumulation; size distribution; water model.

1. Introduction

Argon gas injection is widely used to prevent nozzle clogging during continuous casting of steel. Argon gas is well known to improve clogging resistance via several mechanisms¹⁾ which include preventing deoxidation products/inclusions from contacting the nozzle wall,²⁻⁴⁾ flushing the inclusions off of the nozzle,^{4,5)} promoting the flotation of inclusions,⁶⁾ reducing negative pressure and air aspiration through the nozzle walls,^{4,7,8)} and preventing chemical reactions between the steel and the nozzle refractory.⁶⁾

However, unoptimized argon gas injection may be detrimental to final steel product quality. The annular or slug flows produced by abnormal high gas flow rate compared to the molten steel flow rate in a nozzle can produce asymmetric jet flow in the mold,^{9,10)} shallower jet angle,¹¹⁾ and higher turbulence energy,¹¹⁾ resulting in severe surface velocity and level fluctuations,¹²⁾ and finally causing surface defects in the final steel products.⁹⁻¹²⁾ In addition, abnormal big bubbles easily float upwards to the surface near

a Submerged Entry Nozzle (SEN), which may cause slag entrainment into the molten steel pool there.^{13,14)} Finally, bubbles can be entrapped into the solidifying steel shell, especially those smaller than the primary-dendrite arm spacing.^{15,16)} This can lead to bubble-related defects, including segregation,¹⁷⁾ blisters,^{10,18)} and slivers from the associated inclusions covering the bubble surface.¹⁸⁾

To decrease these bubble related defects, it is important to better understand bubble behavior, including their size distribution in the nozzle and mold. Argon gas can be injected in several ways, including through small holes or porous refractory in the Upper Tundish Nozzle (UTN) and/or the SEN. Liu and Thomas developed a validated gas flow model, and applied the model to investigate the gas distribution on the UTN refractory surface, gas mass flow rate, and leakage fraction through the UTN refractory with the slide-gate system.¹⁹⁾ Lee *et al.* found the empirical correlation between gas injection parameters and active sites on the UTN refractory.²⁰⁾ Other methods to inject argon gas into the molten steel in the nozzle is through joints in the sliding gate, or through porous brick or gas channels in or near to the stopper-rod tip. Injecting gas through a single channel in the center of the stopper tip²¹⁻²³⁾ is a popular method.

* Corresponding author: E-mail: bgthomas@mines.edu
 DOI: <http://dx.doi.org/10.2355/isijinternational.ISIJINT-2018-096>

However, this method often creates abnormal large bubbles or gas pockets²³⁾ due to the low pressure and stagnant flow conditions. These large bubbles and gas pockets are well known to produce slug or annular flows in the nozzle, leading to flow instabilities, mold level fluctuations, and product quality problems.^{9,10)} To reduce the flow fluctuations in the mold associated with the single channeled stopper-rod, gas injection using a multi-channeled stopper-rod has been developed.^{24–27)} Gas bubbles injected through multiple channels in the side of the stopper tip produce more stable surface level in the mold and lessens clogging buildup on the stopper-rod tip, which is a common problem in casting aluminum-killed steel with a stopper-rod using a porous refractory tip for gas injection.²⁷⁾

Investigations of gas bubble size in continuous casting are relatively rare. A few previous studies have measured bubble distributions in the final solidified slab.^{28–30)} Other studies have measured air-bubble size distributions in the nozzle^{20,31–33)} and mold^{34–39)} during casting, using water model experiments and mathematical modeling. The average bubble size ranges from 2–6 mm initial diameter, 0.5–3.5 mm inside the SEN, and 1–3 mm in the mold, for various conditions including water and air flow rates and geometries. Due to the higher surface tension, the size of argon bubbles injected into liquid metal is expected to be larger than that in equivalent air-water systems.³¹⁾ One study of argon and liquid GaInSn metal in a high-aspect ratio (thin) physical model of stopper-rod system, measured argon bubble size distributions, showing 1–10 mm diameter range in the mold.²³⁾ Another study that measured argon bubble size distributions, in a Wood’s metal model of the continuous-casting mold, found exponentially more small bubbles than large bubbles at the meniscus.⁴⁰⁾

In the present work, the behavior and size distributions of bubbles, injected through a stopper rod with multiple downward-inclined channels in its tip, are investigated using 1/3-scale water-model measurements and analytical model predictions. Bubble formation at the gas channel exits and bubble behavior in the nozzle and mold regions are quantified by visualizing the phenomena using a high-speed video camera and analyzing those phenomena, including calculations of threshold pressure for bubble formation, initial bubble size, bubble terminal descending velocity, residence time, and changes in bubble size distribution due to bubble accumulation. Furthermore, bubble size distributions in the nozzle and mold, are measured by image-analyzing each snapshot from the video recording. The model of initial bubble formation is validated via comparisons with the water model measurements, and finally is extended to estimate argon bubble size in the molten steel caster.

2. Water Model Experiments

To investigate argon bubble behaviors and size distributions in the nozzle and mold during continuous casting of steel, water-air system experiments were conducted using a 1/3rd scale water model of a continuous slab caster, shown in **Fig. 1**. The model consists of the tundish, stopper-rod, SEN, and mold. Vertical movement of the stopper-rod controls the water flow rate from the tundish through the SEN into the mold, by changing the size of the annular gap between the

stopper end and the bottom of the tundish where it curves into the SEN. Water exits holes in the bottom of the mold to a holding water bath and is pumped continuously back up to the tundish. Dimensions and process conditions for both the real caster and the water model are given in **Table 1**. The casting speed was chosen based on maintaining a constant Froude number, which is defined as the ratio of inertia force to gravitational force as follows.

$$\left(U_W / \sqrt{gL_W} \right) = \left(U_R / \sqrt{gL_R} \right) \dots\dots\dots (1)$$

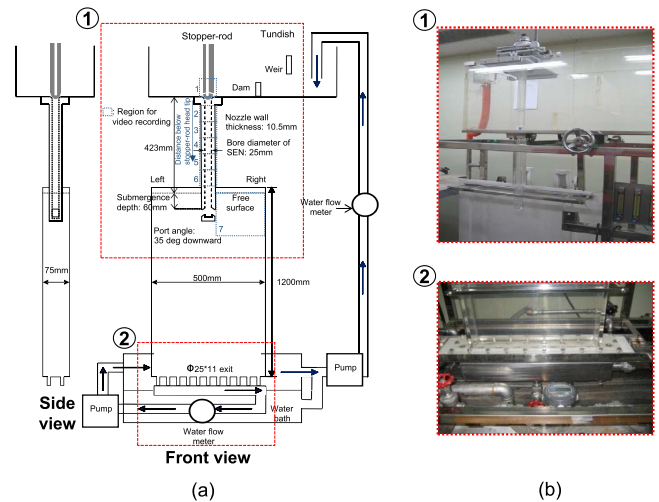


Fig. 1. (a) Schematic and (b) photos of the 1/3 scale water model. (Online version in color.)

Table 1. Caster dimensions and process conditions.

	Real caster	1/3 scale water model
Dimensions		
Nozzle bore inner diameter	75 mm	25 mm
Nozzle bore outer diameter	138 mm	46 mm
Nozzle bottom well depth	18 mm	6 mm
Nozzle port width	69.9 mm	23.3 mm
Nozzle port height	80.1 mm	26.7 mm
Nozzle port angle		–35° (down) angle
Tundish level, $H_{tundish}$	1 020 mm	340 mm
Distance from nozzle inlet to nozzle port	1 449 mm	483 mm
Mold thickness	225 mm	75 mm
Mold width	1 500 mm	500 mm
Process conditions		
Steel flow rate	Q_R : 545.6 LPM	Q_W : 35 LPM
Casting speed	$U_{Casting,R}$: 1.61 m/min	$U_{Casting,W}$: 0.93 m/min
Gas flow rate*	Cold (at 273 K): $q_{R(273 K)}$: 0.8 , 1.5, 2.3, 3.1 , 3.8, 4.6, 5.4, 6.1 SLPM	At 298 K: q_W : 0.2 , 0.4, 0.6, 0.8 , 1.0, 1.2, 1.4, 1.6 LPM
	Hot (at 1 873 K): $q_{R(1 873 K)}$: 3.1 , 6.2, 9.4, 12.5 , 15.6, 18.7, 21.8, 24.9 LPM	
Gas volume fraction (hot)*	0.6 , 1.1, 1.7, 2.2 , 2.8, 3.3, 3.8, 4.4 %	
Submerged depth of nozzle	165 mm	55 mm

* The 3 cases in **bold** were investigated in detail in the nozzle and mold.

where W is for water model, R is for real caster, U is a typical speed, L is a typical dimension, and g is gravitational acceleration. The equation was rearranged to find the casting speed in the water model, $U_{Casting,W}$ as follows.

$$U_{Casting,W} = U_{Casting,R} \sqrt{L_W / L_R} \dots\dots\dots (2)$$

Air gas is injected through gas channels near the bottom of the stopper-rod, shown in Fig. 2(a). Gas flows down a main central circular-channel (D_{mc} : 10 mm) inside the stopper-rod. From the main gas channel, 6 branch circular-channels (D_{bc} : 1 mm) with a downward vertical-angle (θ_v) of 15° are placed at equal intervals of a horizontal angle (θ_h : 60°), towards the stopper-rod head side-walls. Each exit of these branch channels is located at $H_{bc} = 10$ mm above the tundish-bottom for 35.0 LPM, which is the water flow-rate condition for this work. Geometric details are given in Table 2.

Air flow rate in the water model was chosen to maintain a constant gas volume fraction as follows.

$$\frac{q_W}{Q_W + q_W} = \frac{q_{R(1873K)}}{Q_R + q_{R(1873K)}} = \frac{\lambda q_{R(273K)}}{Q_R + \lambda q_{R(273K)}} \dots\dots\dots (3)$$

where Q_W is water volume flow rate, Q_R is molten-steel volume flow rate, q_W is air volume flow rate at 298 K, $q_{R(1873K)}$

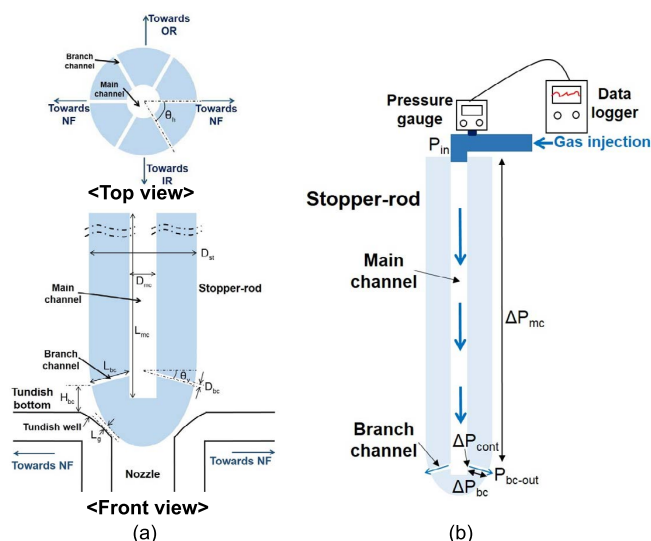


Fig. 2. (a) Schematic of the stopper-rod with multi-channels for gas injection, (b) gas injection through the stopper-rod and measurement of gas pressure in the water model. (Online version in color.)

Table 2. Dimensions of the stopper-rod with the gas channels.

Dimension	Value
Diameter of stopper-rod: D_{st}	42 mm
Diameter of main gas channel: D_{mc}	10 mm
Diameter of branch gas channel: D_{bc}	1 mm
Length of main gas channel: L_{mc}	517.3 mm
Length of branch gas channel: L_{bc}	15.7 mm
Gap size between stopper and tundish well: L_g	2 mm
Vertical-angle of branch channel: θ_v	15° (downward angle)
Horizontal-angle of branch channel: θ_h	60°
Height from tundish bottom to branch channel exit: H_{bc}	10 mm (for water flow rate 35 LPM)

is argon volume flow rate at 1 873 K, $q_{R(273K)}$ is argon gas volume flow rate at standard conditions (1 atm, 273 K), and λ is gas expansion factor. Because argon gas injected into the molten steel pool is greatly affected by the high temperature of the molten steel and pressure at the branch channel exit, λ is calculated as follows.

$$\lambda = \frac{q_{R(1873K)}}{q_{R(273K)}} = \frac{\rho_{R(273K)}}{\rho_{R(1873K)}} = \left(\frac{P_{273K}}{P_{1873K}} \right) \times \left(\frac{1873K}{273K} \right) = \left(\frac{P_{273K}}{P_{s,tundish_level} + \rho_s g (H_{tundish} - H_{bc})} \right) \times \left(\frac{1873K}{273K} \right) \dots\dots\dots (4)$$

where, $\rho_{R(273K)}$ is argon gas density at standard conditions (1 atm, 273 K), $\rho_{R(1873K)}$ is argon gas density at 1 873 K, P_{273K} is 1 atm, and P_{1873K} is molten steel pressure at the branch gas channel exits. $P_{s,tundish_level}$ is pressure at the top surface of the tundish (1 atm), ρ_s is molten steel density, and $H_{tundish} - H_{bc}$ is hydrostatic pressure head distance from the top surface to the branch-channel exit in the tundish. In this work, λ is 4.1, based on fluid properties for both molten steel-argon gas and water-air systems given in Table 3.

Once the water-air flow reached steady state in the stopper-rod nozzle and mold, bubble behaviors in the nozzle (Regions 1–6) and mold (Region 7) were captured using a high-speed video camera at 1 200 frames/s. The recorded image snapshots were analyzed using the image-analysis program, Image J,⁴¹⁾ to quantify the size distributions of the bubbles in each analysis window. As shown in Fig. 3, a scale was set in each original image, and the size of all bubbles in the analysis window was identified by transforming the photo into a binary image and measuring the areas. In addition, during gas injection, instantaneous gas pressure at the main channel inlet was measured every 0.01 s for 10 s using a pressure gauge with 0.05 kPa pressure resolution and a data logger as shown in Fig. 2(b).

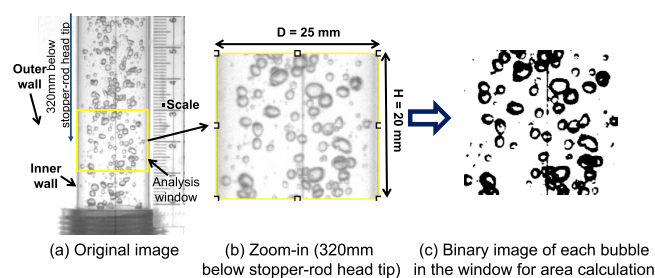


Fig. 3. Bubble size image analysis. (Online version in color.)

Table 3. Comparison of physical properties between molten steel-hot argon and water-air systems.

	Molten steel-hot argon system	Water-air system
Liquid density: ρ_l	7 000 kg/m ³	998.2 kg/m ³
Gas density: ρ_g	Cold (at 273 K): 1.623 kg/m ³ Hot (at 1 873 K): 0.399 kg/m ³	At 298 K: 1.225 kg/m ³
Liquid dynamic viscosity: μ_l	0.007 kg/m·s	0.001 kg/m·s
Gas dynamic viscosity: μ_g	2.1×10^{-5} kg/m·s	1.8×10^{-5} kg/m·s
Interfacial tension coefficient: σ	1.192 N/m	0.073 N/m

3. Analytical Models

To quantify bubble behaviors in the nozzle and mold, four analytical models were applied to calculate gas pressure at the main channel inlet, initial bubble size at the branch channel exit, bubble terminal descending velocity in the nozzle, and bubble size distribution changes expected based on accumulation inside the nozzle.

3.1. Gas Pressure for Bubble Initiation

Bubbles are modeled to form at the branch channel exits in four stages of initiation, expansion, elongation, and detachment stages, as shown in Fig. 4. To initiate the bubble formation (Fig. 4(a)), gas pressure at the branch channel exit around the liquid pool in the tundish bottom, P_{bc-out} must overcome the liquid hydrostatic pressure, P_{hyd} and a threshold pressure based on the maximum surface tension force, $\sigma\kappa_{max}$, as given in Eq. (5) following the Young-Laplace equation.⁴²⁾

$$P_{bc-out} = P_{hyd} + \sigma\kappa_{max} \dots\dots\dots (5)$$

Considering the pressure drop from the main channel inlet to the branch channel exit, the pressure at each branch channel exit is given by Bernoulli's equation as follows.

$$P_{bc-out} = P_{in} + \frac{1}{2}\rho_g(u_{mc}^2 - u_{bc}^2) + \rho_g g(H_{mc} - H_{bc}) \dots (6)$$

$$-\Delta P_{channels}$$

where P_{in} is inlet gas pressure at the top of the main channel, ρ_g is gas density, u_{mc} is gas velocity in the main channel, u_{bc} is gas velocity in the branch channel, H_{mc} is height from the tundish bottom to the main channel inlet, H_{bc} is height from the tundish bottom to the branch channel exit, and $\Delta P_{channels}$ is total pressure drop including three pressure drops: across the main channel, across a branch channel and due to sudden contraction of the cross-sectional area from the main channel to the branch channel.

Rearranging the above equations gives the minimum pressure at the main channel inlet, P_{in} , that is needed to exceed the threshold pressure at the exit of at least one branch channel and initiate gas bubble formation:

$$P_{in} = P_{hyd} + \sigma\kappa_{max} - \frac{1}{2}\rho_g(u_{mc}^2 - u_{bc}^2) \dots\dots\dots (7)$$

$$-\rho_g g(H_{mc} - H_{bc}) + \Delta P_{channels}$$

Hydrostatic pressure at the branch channel exit in the tundish bottom region, P_{hyd} is calculated as follows.

$$P_{hyd} = \rho_l g(H_{tundish} - H_{bc}) \dots\dots\dots (8)$$

where ρ_l is liquid density, $H_{tundish}$ is height of the top-surface water level above the tundish bottom.

Surface tension force is maximum with the largest bubble-surface curvature when the hemisphere bubble diameter equals the branch channel diameter.

$$\sigma\kappa_{max} = \frac{2\sigma}{r_{bc}} \dots\dots\dots (9)$$

where r_{bc} is radius of the branch channel exit.

Pressure drop in the system is calculated as follows.

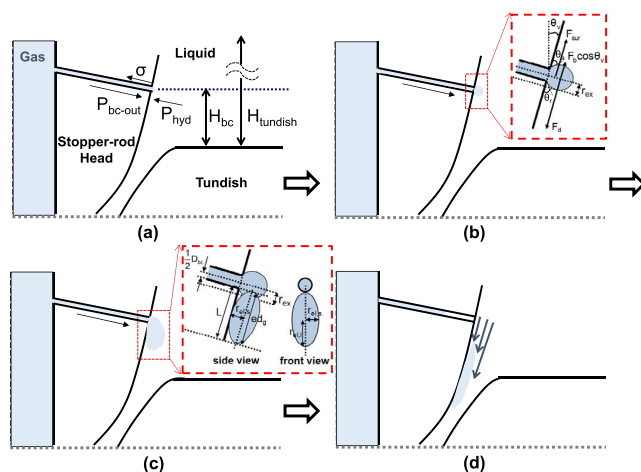


Fig. 4. Bubble formation mechanism: (a) initiation, (b) expansion, (c) elongation, and (d) detachment. (Online version in color.)

$$\Delta P_{channels} = \Delta P_{mc} + \Delta P_{bc} + \Delta P_{cont}$$

$$= \frac{128\mu_g}{\pi} \left(\frac{L_{mc}q_{g,mc}}{(D_{mc})^4} + \frac{L_{bc}q_{g,bc}}{(D_{bc})^4} \right) \dots\dots (10)$$

$$+ \frac{1}{2}\rho_g \left(0.42 \left(1 - \frac{(D_{bc})^2}{(D_{mc})^2} \right) \right) (u_{bc})^2$$

where ΔP_{mc} is pressure drop across the main channel, ΔP_{bc} is pressure drop across each branch channel, calculated using the Hagen-Poiseuille equations,⁴³⁾ ΔP_{cont} is pressure drop due to the sudden area contraction between the two channels,⁴³⁾ μ_g is gas dynamic viscosity, D_{mc} is main channel diameter, D_{bc} is branch channel diameter, L_{mc} is main channel length, L_{bc} is branch channel length, $q_{g,mc}$ is total gas volume flow rate in the main channel, and $q_{g,bc}$ is gas volume flow rate in each branch channel ($q_{g,mc}/6$).

3.2. Initial Bubble Size

Video observations show how the initial gas bubbles form at the branch channel exits in the stopper rod. After initiating bubble formation, the gas bubble protruding from the channel exit expands and elongates as shown in Figs. 4(b) and 4(c). Then, the bubble is detached from the stopper-rod wall due to the shearing drag forces of the fast liquid flow through the gap between the nozzle inlet and the stopper-rod head region. To calculate this initial bubble size, a semi-analytical model of bubble formation in downstream flow by Bai and Thomas³¹⁾ was applied, using the process parameters for the current stopper-rod gas-injection flow system.

During the expansion stage, Fig. 4(b), the bubble sits on the tip of the gas channel exit and is assumed to maintain a spherical shape, obeying the following force balance including drag force F_d (left term), buoyancy/gravity force F_b (right first term), and surface tension force F_{sur} (right second term),

$$\frac{1}{2}C_d\rho_l(\bar{u}_l)^2\pi(r_{ex})^2 = \frac{4}{3}\pi(r_{ex})^3(\rho_l - \rho_g)g\cos\theta_v \dots (11)$$

$$+ \frac{1}{2}\pi r_{ex}\sigma f_\theta(\bar{u}_l)$$

where C_d is drag coefficient according to Reynolds number,⁴⁴⁾ ρ_l is liquid density, \bar{u}_l is steady average liquid veloc-

ity across expanding bubble, r_{ex} is expanded radius of the gas bubble to be solved, ρ_g is gas density, g is acceleration of gravity, θ_v is vertical angle of the branch channel, σ is surface tension coefficient, and f_θ is a contact angle function that depends on the static contact angle and difference between contact angles (advancing contact angle, θ_a and receding contact angle, θ_r) above and below the bubbles.³¹⁾

In the elongation stage (Fig. 4(c)), the bubble elongates along the stopper-rod surface when the drag force starts to exceed the surface tension and buoyancy force. Thus, the bubble has an ellipsoid shape at the stopper-rod head surface, due to this shearing effect of the flowing liquid. The equation³¹⁾ to predict final bubble size, $d_g (= 2r_{el,s} \sqrt{e})$ just before it detaches from the stopper-rod head is given as follows.

$$5.2692 \frac{\pi U_{tum}}{q_{g,bc} (D_{tum})^{1/7}} \int_{r_{ex}}^{r_{el,s}} \left(r^{15/7} (ar+b)^{3/2} + \frac{ar^{22/7}}{2} (ar+b)^{1/2} \right) dr$$

$$= 2r_{el,s} (e)^{3/2} + \frac{D_{bc}}{2} - r_{ex} \dots \dots \dots (12)$$

where $q_{g,bc}$ is average gas volume flow rate into each active branch channel ($q_{g,mc}/n_{act}$), n_{act} is number of activated branch channels, U_{tum} is average liquid velocity near the branch channel exit, D_{tum} is hydraulic diameter in the tundish bottom region, a and b are constants related with r_{ex} , the expansion radius, $r_{el,s}$, the horizontal radius of the elongated bubble to be solved, and e , the elongation factor of the bubble.³¹⁾

3.3. Bubble Terminal Descending-Velocity

To calculate the residence times of bubbles in the nozzle, the bubble terminal descending-velocity, $u_{g,terminal,i}$ is calculated from a force balance between the drag force and the buoyancy/gravity force on each gas bubble size as follows.

$$\frac{1}{2} \rho_l (u_l - u_{g,terminal,i})^2 C_d A_i = \frac{1}{6} (d_{g,i})^3 (\rho_l - \rho_g) g \dots (13)$$

where ρ_l is liquid density, ρ_g is gas density, $d_{g,i}$ is gas bubble diameter i , u_l is liquid velocity in the nozzle, A_i is cross sectional area, which is calculated as $\pi (d_{g,i})^2 / 4$, and C_d is drag coefficient which varies with relative Reynolds number and Weber number for the tap water-air system as follows.⁴⁵⁾

$$C_d = \begin{cases} \frac{16}{Re}, & Re < 0.49 & (Range\ 1) \\ \frac{20.68}{Re^{0.643}}, & 0.49 < Re < 100 & (Range\ 2) \\ \frac{6.3}{Re^{0.385}}, & 100 < Re & (Range\ 3) \dots (14) \\ \frac{We}{3}, & \frac{2\ 065.1}{We^{2.6}} < Re & (Range\ 4) \\ \frac{8}{3}, & 8 < We & (Range\ 5) \end{cases}$$

where $Re = \frac{\rho_l d_{g,i} |u_{g,terminal,i} - u_l|}{\mu_l}$, $We = \frac{\rho_l d_{g,i} |u_{g,terminal,i} - u_l|^2}{\sigma}$, and μ_l is liquid dynamic viscosity.

Rearranging Eq. (13) gives the terminal descending velocity of each bubble size, $u_{g,terminal,i}$ as follows

$$u_{g,terminal,i} = \frac{Q_l}{A_{nozzle}} - \sqrt{\frac{4(\rho_l - \rho_g) d_{g,i}}{3 \rho_l C_d} g} \dots \dots \dots (15)$$

where Q_l is liquid flow rate in the nozzle and A_{nozzle} is cross-sectional area of the nozzle.

3.4. Bubble Size Distribution Based on Accumulation

Changes in the bubble size distribution due to gas accumulation in the nozzle were simply estimated based on terminal descending velocity of each bubble size. Inside the nozzle between Regions 3 and 6, the total number of bubbles of each diameter, $n_{3-6,i}$ was predicted based on the bubble size distribution measured in Region 3, $n_{3,i}$ as follows.

$$n_{3-6,i} = n_{3,i} f t_{residence,i} \dots \dots \dots (16)$$

where i is bubble diameter, f is bubble frequency, $t_{residence,i}$ is residence time of a bubble between Regions 3 and 6,

$$t_{residence,i} = \frac{L_{3-6}}{u_{g,terminal,i}} \dots \dots \dots (17)$$

where L_{3-6} is vertical distance from Region 3 to 6. From the total number of bubbles of each diameter calculated to reside within Regions 3–6, the number of bubbles in Region 6, $n_{6,i}$ was estimated as follows.

$$n_{6,i} = \frac{L_6}{L_{3-6}} n_{3-6,i} \dots \dots \dots (18)$$

where L_6 is the vertical height of the analysis window in Region 6. Finally, the population proportion of each bubble diameter in Region 6, $P_{6,i}$, is calculated as follows.

$$P_{6,i} = \frac{n_{6,i}}{\sum_{i=1}^n n_{6,i}} \times 100 = \frac{\frac{n_{3,i}}{u_{g,terminal,i}}}{\sum_{i=1}^n \frac{n_{3,i}}{u_{g,terminal,i}}} \times 100 \dots \dots \dots (19)$$

4. Results and Discussion

Bubble behavior and size distributions in the nozzle and mold are investigated by quantifying bubble formation, bubble frequency, initial bubble size, breakup, coalescence, and accumulation phenomena by applying both water model measurements and analytical model predictions.

4.1. Bubble Formation, Frequency, and Initial Size

The number of activated branch channels for bubble formation was measured from the video recordings for various gas flow rates, and given in Fig. 5. At lower gas flow rates, not all of the branch channels are activated simultaneously. The number of activated channels generally increases with higher gas flow rate. All six gas-channels are activated when the gas flow rate exceeds a critical value, which is between 1.4 and 1.6 LPM. It is likely that slightly non-uniform pressure drops across the branch channels or asymmetric flow near the channel exit in the tundish causes this phenomenon. When the gas flow rate barely exceeds the minimum threshold, only the single branch channel with the largest diameter is able to generate bubbles, which inhibits the system pressure from building up. A significant increase in

flow rate is required to increase the system pressure enough to overcome the pressure threshold in the next largest branch channel, and so on.

Histories of gas pressure at the main gas channel inlet were measured for 10 s of steady bubble formation for various gas flow rates. An example is shown in Fig. 6. The observed variations are due to the intermittent detachment of bubbles from the channel exits. The gas pressure drop in the system mainly occurs through the branch channels, which account for ~ 84% of the total pressure drop, as shown in Fig. 7. Average (symbols) and standard deviation (error bars) of the measured pressure at the main channel inlet are given in Fig. 8 for several gas flow rates and are compared with the predicted pressure threshold for bubble formation at the same location. Both the measurements and the predictions show that higher gas flow rate increases gas pressure at the channel inlet. The predicted pressure threshold increases with flow rate due to the larger pressure drop across the branch channel. The measured average pressure

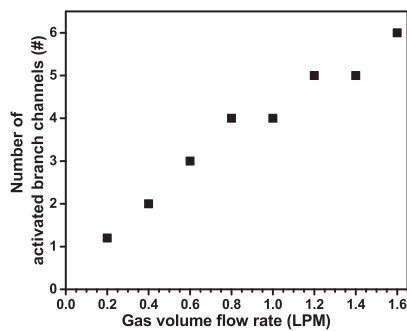


Fig. 5. Effect of gas volume flow rate on activation of the branch channels for bubble formation in the water model.

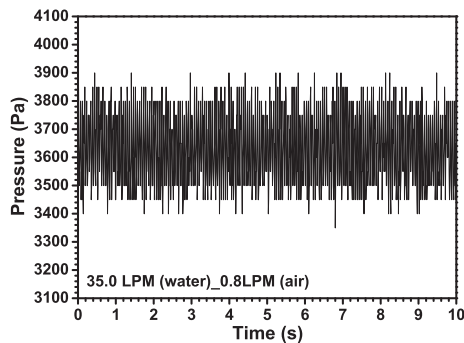


Fig. 6. Measurement of gas pressure at the main gas-channel inlet for 35.0 LPM (water) with 0.8 LPM (air).

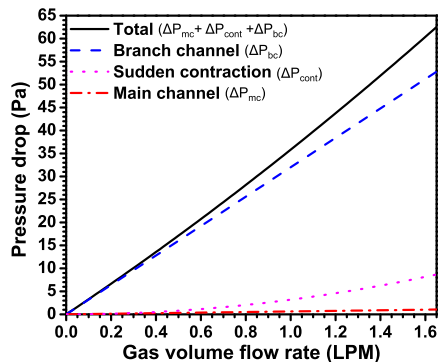


Fig. 7. Calculated pressure drop in the gas channels. (Online version in color.)

is slightly greater than the predicted pressure threshold as expected, in order to enable flow. The difference generally increases with increasing flow rate, except for jumps when flow through a new branch channel is activated.

After passing through the channels, gas at the branch channel exit faces liquid flow, and can form bubbles only if the gas pressure can overcome the hydrostatic pressure of the liquid and surface tension force. The total frequency of bubble formation increases with increasing gas flow rate, as shown in Fig. 9. However, as more channels become activated, the frequency per branch channel is always ~100/s, which means that the formation of one bubble takes ~0.01 s. With increasing gas flow rate, this frequency decreases slightly, which causes the bubble size to increase slightly. Based on the measured total bubble frequency, f , the initial volume-averaged bubble diameter at the branch channel exit, $d_{avg,g}$, can be calculated as follows,

$$d_{avg,g} = \left(\frac{6q_{g,mc}}{\pi f} \right)^{\frac{1}{3}} \dots\dots\dots (20)$$

where $q_{g,mc}$ is gas flow rate into the main gas channel.

These average initial bubble sizes measured in the water model at several gas flow rates are compared in Fig. 10 with the analytical model predictions of d_g using Eqs. (11) and (12) and with several empirical models suggested by other researchers,⁴⁶⁻⁴⁸ which are given in Table 4. As shown in Fig. 10, the empirical models for stagnant liquid flow systems over-predict the initial bubble diameter at the branch channel exit in the stopper-rod. This is expected because in the current work, the shearing effect from the high velocity liquid flowing into the gap between the tundish bottom and

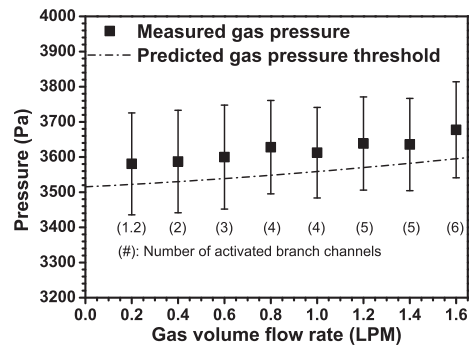


Fig. 8. Comparison of predicted gas pressure threshold with measured gas pressure at the main channel inlet in the water model.

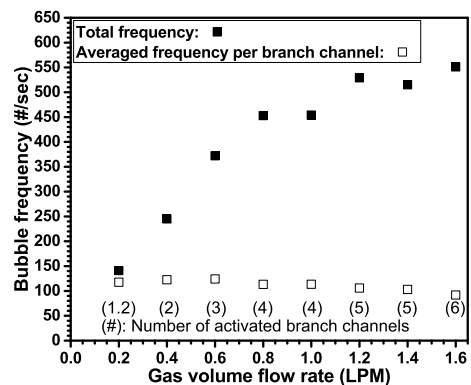


Fig. 9. Effect of gas volume flow rate on bubble frequency in the water model.

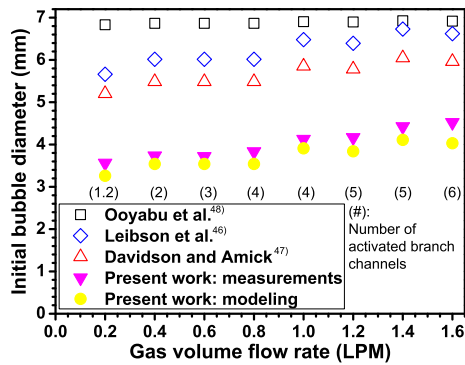


Fig. 10. Initial bubble size at the branch channel exit in the water-air model. (Online version in color.)

Table 4. Empirical models to predict average initial bubble-size.

Single-channel bottom injection in stagnant flow	
Leibson <i>et al.</i> ⁽⁴⁶⁾	$d_g = 0.91 (D_{bc})^{1/2} (Re)^{1/3}$ where D_{bc} : 0.4–3 mm, $Re = \frac{4\rho_g q_{g,mc}}{\pi\mu_g n_{act} D_{bc}}$: 300–2 100
Davidson and Amick ⁽⁴⁷⁾	$d_g = 8.75 \left\{ \left(\frac{q_{g,mc}}{n_{act}} \right) (D_{bc})^{0.5} \right\}^{0.29}$ where D_{bc} : 0.34–15.8 mm, $\frac{q_{g,mc}}{n_{act}}$: 0.0006–15 LPM
Multi-channels side injection in stagnant flow	
Ooyabu <i>et al.</i> ⁽⁴⁸⁾	$d_g = 31.2 \left(k^{-1/3} \left(\frac{q_{g,mc}}{n_{act}} \right)^{1/3} \left(\frac{\rho_l P_g^4}{\sigma^5} \right)^{-1/60} \left[0.32 \left\{ \left(\frac{q_{g,mc}}{n_{act}} \right)^2 \frac{1}{g} \right\}^{-1/15} D_{bc}^{1/3} \right]^n$ where $k = 0.837 + 0.805 \log \left(\frac{D_{bc}}{D_{mc}} \right)$ and $n = 0.54 \left(\frac{D_{bc}}{D_{mc}} \right)^{-0.63}$

the stopper-rod shortens the time of bubble formation and results in smaller bubbles with higher bubble frequency. In contrast, the predicted bubble diameter using the two-stage analytical model shows much better agreement with the measurements. This is because the analytical model was formulated for gas injection into downward flowing liquid, such as encountered in the current flow system. Thus, the analytical model is validated, and can be applied to molten steel-argon gas system in the real plant.

4.2. Breakup, Coalescence, and Accumulation in Nozzle

Bubbles formed at the gas branch-channel exit enter into the highly turbulent flow field in the ~ 2 mm gap between the stopper-rod head and the tundish bottom. As shown in **Fig. 11**, bubble size drastically decreases, from an average initial size of ~ 4.5 mm to only ~ 1 mm after passing through the gap into Region 2 in the upper SEN. In the narrow gap region, two mechanisms cause the bubbles to break up. First, the narrow gap forces the bubbles to elongate and the accompanying high velocity gradients cause high shear forces which tear the bubbles apart. In addition, the high turbulent kinetic energy of eddies smaller than the bubble size contributes further to the breakup. This is why the bubbles in the SEN are much smaller than the initial bubbles formed at the branch channel exits.

In the nozzle, multiple bubbles were observed to collide and coalesce in complex manners during their flow downward. Some examples of this bubble coalescence behavior

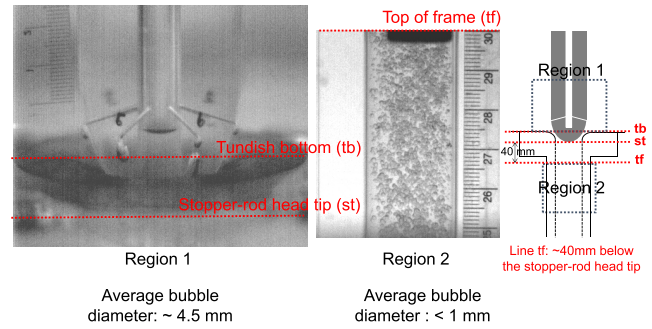


Fig. 11. Bubble breakup in the nozzle inlet region near the stopper-rod tip: 35.0 LPM (water) and 1.6 LPM (air). (Online version in color.)

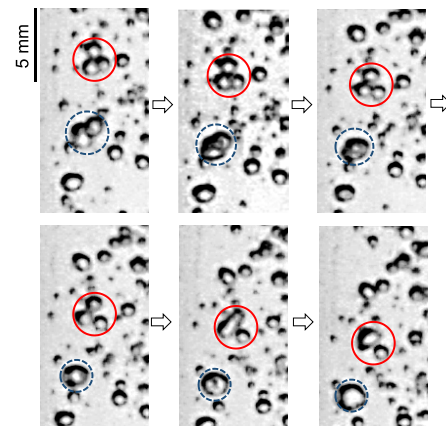


Fig. 12. Example of bubble coalescence in the nozzle region 150–160 mm below the stopper-rod head tip ($833 \mu\text{s}$ between the snapshots): 35.0 LPM (water) and 0.2 LPM (air). (Online version in color.)

are shown in **Fig. 12** for a ~ 4.2 ms time period. The solid red and dashed blue circles identify two kinds of coalescence phenomena, which were commonly observed in the upper SEN for bubbles smaller than 1.5 mm diameter. The solid red circles show three bubbles touching, causing two of the bubbles to coalesce while the third bubble bounces away. On the other hand, the dashed blue circles show three different bubbles all coalescing into one big bubble. This shows that bubble collisions sometimes produce coalescence, which is an important mechanism to increase the average bubble size in the nozzle.

During downward flow in the nozzle, a second mechanism contributes to the bubble size distribution evolving towards larger sizes. Big bubbles have lower descending velocity in the downward liquid flow. Specifically, **Fig. 13** shows how terminal descending velocity of bubbles decreases with increasing bubble diameter up to 2.3 mm, as calculated using Eq. (15). Bubbles larger than 2.3 mm diameter have ~ 0.96 m/s terminal descending velocity, which is $\sim 20\%$ lower than the mean liquid flow velocity (~ 1.2 m/s). This buoyancy effect causes larger bubbles to have longer residence times in the nozzle, and to accumulate with distance down the nozzle, relative to smaller bubbles.

To illustrate this effect, the residence times in the nozzle of each bubble size are calculated from their terminal descending velocities using Eq. (17), replacing L_{3-6} with the total vertical length of the nozzle. As shown in **Fig. 13**, residence times of the bubbles increase according to the decrease of their descending velocity. Bubbles larger than

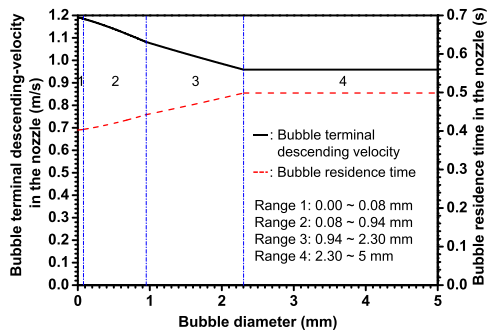


Fig. 13. Bubble terminal descending-velocity and residence time in the water-air SEN. (Online version in color.)

2.3 mm diameter have ~ 20% longer residence time in the nozzle than 0.5 mm diameter bubbles. Thus, both the bubble coalescence phenomenon, and the accumulation of larger bubbles due to their longer residence time in the nozzle, are expected to cause the bubble size distribution inside the nozzle to increase with distance down the SEN.

4.3. Bubble Size Distributions in Nozzle and Mold

Bubbles moving down in four regions (Regions 3–6) separately in the nozzle were recorded using a high speed video. Example snapshots are shown in Fig. 14. Bubble size is observed to increase with distance down the nozzle for both gas flow-rate cases. To quantify the bubble size distributions in the nozzle and mold, Sauter mean diameter d_{32} is calculated in each analysis window as follows:

$$d_{32} = \frac{(d_{avg,V})^3}{(d_{avg,A})^2} = \frac{\sum_{i=1}^n (d_i)^3}{\sum_{i=1}^n (d_i)^2} \dots\dots\dots (21)$$

where d_i is measured bubble diameter, and n is the total number of bubbles in the analysis window. This equation

uses the volume-average diameter $d_{avg,V} = \sqrt[3]{\frac{6 \sum_{i=1}^n \frac{\pi}{6} (d_i)^3}{n\pi}}$,

and area-average diameter $d_{avg,A} = \sqrt{\frac{\sum_{i=1}^n \pi (d_i)^2}{n\pi}}$.

In addition, the standard deviation of the Sauter diameter σ_b is calculated as follows.

$$\sigma_b = \sqrt{\frac{\sum_{i=1}^n (d_i - d_{32})^2}{n}} \dots\dots\dots (22)$$

Bubble size distributions in the analysis window for each nozzle region with air gas flow rates of 0.8 LPM, are given in Fig. 15. Going down through the nozzle regions, both average size and standard deviations increase, which agrees qualitatively with previous work in a nozzle below a slide gate.³³⁾ This is due to both bubble coalescence and the accumulation of large bubbles in the descending nozzle flow. Between Regions 3 and 4, the number of bubbles smaller than 1.5 mm decreased greatly (by ~53%), likely due to the coalescence mechanism shown in Fig. 12. Correspondingly, bubbles larger than 1.5 mm diameter increased in number by 3× between Regions 3 and 4. By Region 6, bubbles larger

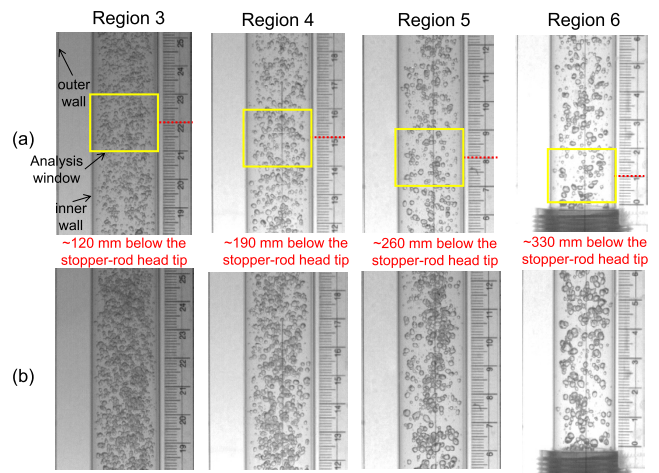


Fig. 14. Bubbles moving down in the nozzle with (a) 35.0 LPM (water) and (a) 0.8 LPM (air) and (b) 1.6 LPM (air). (Online version in color.)

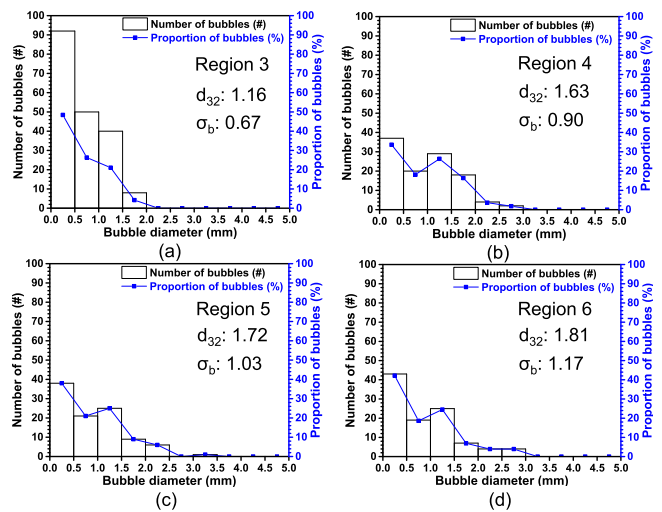


Fig. 15. Bubble size distributions with 35.0 LPM (water) and 0.8 LPM (air) in (a) Region 3, (b) Region 4, (c) Region 5, and (d) Region 6 inside the nozzle. (Online version in color.)

than 2 mm diameter are slightly more frequent than those in Regions 4 and 5. This suggests that small bubble coalescence occurs mainly between Regions 3 and 4, while larger bubbles gradually accumulate with distance down the nozzle.

To compare the relative importance of coalescence and accumulation, the change in bubble size distribution between regions 3 and 6 was predicted using Eq. (19), considering only accumulation, and compared with the measurements in Fig. 16. The predicted proportion of bubbles smaller than 0.5 mm diameter decreases in Region 6, owing to their short residence time. This same trend is observed in the measurements. Correspondingly, bubbles larger than 1 mm accumulate due to their longer residence times, so their proportions increase for both the prediction and measurements. The quantitative discrepancy between the proportion predictions and the measurements is likely due to bubble coalescence inside the nozzle, which appears to be more important than accumulation phenomena.

The bubble size distribution in the mold differs from that in the nozzle due to all three mechanisms of breakup, coalescence, and accumulation. After going down the nozzle to reach the nozzle well bottom and the jet exiting the ports, bubbles experience high turbulence produced by the

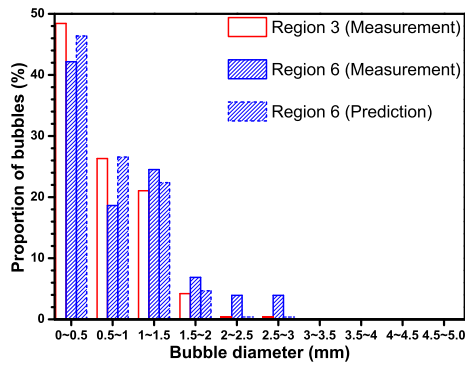


Fig. 16. Bubble accumulation from Region 3 to Region 6 inside the nozzle: 35.0 LPM (water) and 0.8 LPM (air). (Online version in color.)

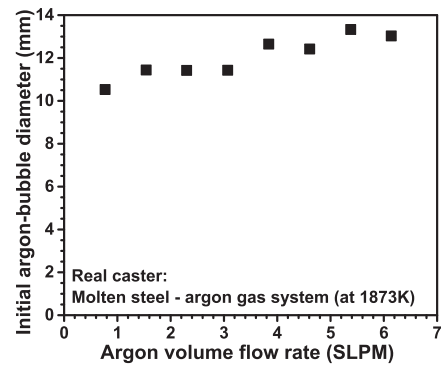


Fig. 18. Predicted initial argon-bubble size in the real caster.

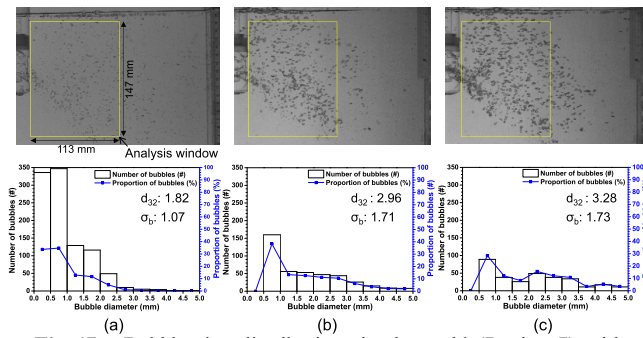


Fig. 17. Bubble size distributions in the mold (Region 7) with 35.0 LPM (water) and (a) 0.2 LPM (air), (b) 0.8 LPM (air), and (c) 1.6 LPM (air). (Online version in color.)

swirling flow, and were observed in the videos to experience breakup. On the other hand, in the upper region of the oversized nozzle ports where flow is stagnant, bubbles were observed to accumulate and coalesce. Then, in the mold, different size bubbles follow different paths and have greatly different residence times. Specifically, smaller bubbles typically have longer residence times and accumulate in the mold more than large bubbles, which exit quickly to the top surface.^{49,50} Measurements of bubble size distributions were taken in the mold for the same casting conditions and 3 gas flow rates (Table 1). Larger average and broader size-range (higher standard deviation of bubble size) of bubble size distribution are produced in the mold, as shown in Fig. 17. In addition, both average and standard deviation of the bubble size in the mold increase with higher gas flow rate. As the breakup and accumulation mechanisms both tend to decrease the average bubble size in the mold, bubble coalescence in the upper port regions is clearly the most important mechanism to explain these measured findings.

4.4. Initial Argon-bubble Size in Molten Steel for Real Caster

The bubble formation model, which was validated by comparing the predicted initial air-bubble size with the water model measurements in Fig. 10, was extrapolated to predict the initial size of argon bubbles in the full-scale steel continuous steel casting system. The steel caster conditions correspond to the water model based on Froude similarity and are included in Table 1. Figure 18 shows that the predicted initial argon bubble size at the branch channel exit of the real stopper-rod is 10.5–13.5 mm, which is much larger than the 3–4 mm air-bubble diameter in the water-air system. Increasing

the gas flow rate per branch gas channel makes bigger argon bubbles, which matches the trend in the air-water system.

The average volume of the initial argon bubbles in the real caster is $\sim 40\times$ larger than the air bubble volume in the water model. This is partly due to the $\sim 15.6\times$ higher argon gas volume flow rate that is needed to maintain the same gas volume fraction in both systems. In addition, surface tension in molten steel-argon gas system is over $16\times$ higher than water-air system. This likely makes the argon bubble stay on the branch channel exit longer in the steel pool and produces larger bubbles, even though molten steel flow has a larger shearing effect, due to its $1.7\times$ higher velocity near the stopper-rod. It is interesting to note, however, that the scaled bubble diameter (dimension) in the steel caster roughly matches the expectation of being $3\times$ bigger, considering the $1/3$ scale factor of the water model.

As investigated from the water-air model measurements, all 3 mechanisms of breakup, coalescence, and accumulation in the nozzle are very significant to determination of the bubble size distributions in the nozzle and mold. Thus, two-phase computational flow models should include all of these complex bubble phenomena, if they aim to predict realistic argon bubble size distributions in the nozzle and mold of the real steel continuous-casting process.

5. Conclusions

Bubble behavior and size distributions in the nozzle and mold of a continuous-casting system with a stopper-rod having six branch channels for gas injection, were investigated during steady casting conditions with $1/3$ -scale water-air model experiments and analytical model predictions. Bubble formation, breakup, coalescence, and accumulation were visualized with a high-speed video-camera and quantified with aid of the model predictions of gas pressure, initial bubble size, bubble terminal descending velocity, bubble residence time, and bubble size distribution considering accumulation in the nozzle. In addition, bubble size distributions in the nozzle and mold were measured with image analysis of video snapshots. The main findings are summarized as follows.

- Gas injected through the multiple channels in this stopper-rod encounter fast downward flow which forms bubbles in four steps: initiation, expansion, elongation, and detachment.
- Bubble formation is initiated when the inlet gas pressure exceeds the threshold pressure that consists of the pressure drops across the gas channels and due to the sudden area

contraction between the gas channels, the hydrostatic pressure from the liquid level in the tundish, and the surface tension force at the branch-channel exit. A higher threshold is needed to produce flow through all 6 branch channels, which are activated in sequence as the gas flow rate is increased.

- With higher gas flow rate, more channels becoming activated decreases the bubble frequency exiting each channel slightly, so the average initial bubble size increases slightly.

- Bubbles detach from the stopper-rod head and flow into the gap between the stopper-rod head and the nozzle inlet, where they become elongated and torn due to the narrow gap, high velocity gradients and high turbulence. This significant bubble breakup results in much smaller bubble size in the region just below the nozzle inlet.

- While flowing down the nozzle, small bubbles collide in complex manners and coalesce while larger bubbles accumulate due to their longer residence time. Both mechanisms lead to increasing bubble size with distance down the nozzle, although coalescence is more important.

- In the nozzle well bottom and jet, bubbles breakup due to the high turbulence. In the stagnant upper region of the nozzle port, bubbles coalesce. In the mold, small bubbles accumulate. Measured bubble size distributions in the mold are larger and have a broader size range, compared with those in the nozzle, indicating that coalescence is the dominant mechanism.

- In both the nozzle and mold regions, the average and standard deviation of the bubble size increases with increasing gas flow rate.

- The semi-analytical model of bubble formation that considers expansion and elongation stages shows good agreement with the initial air-bubble size measured in the water model at stopper-rod branch channel exit.

- Applying the validated two-stage bubble-formation model to argon gas bubbles in the real steel caster predicts much larger ($\sim 3\times$) bubbles, relative to those in the water-air model, as expected considering the 1/3 scale factor.

- The injection of argon gas through multiple branch channels in the sides of the stopper rod tip is expected to be better than single-channel injection of high gas flow rates through the center of the stopper-rod tip, by producing more stable bubbly flow in the nozzle, avoiding annular/slug flow, and leading to less transient surface-level variations in the mold.

Acknowledgements

The authors thank POSCO and Shin-Eon Kang, POSCO Technical Research Laboratories for providing the water model, and Dae-Woo Yoon, POSTECH for help with the 1/3 scale water model experiments. Supports from the Continuous Casting Consortium at University of Illinois at Urbana-Champaign, the Continuous Casting Center at Colorado School of Mines, POSCO, South Korea (Grant No. 4.0002397), and the National Science Foundation GOALI grant (Grant No. CMMI 15-63553) are gratefully acknowledged.

REFERENCES

- 1) K. Rackers and B. G. Thomas: Proc. 78th Steelmaking Conf., Vol. 78, Iron and Steel Society, Warrendale, PA, (1995), 723.
- 2) T. R. Meadowcroft and R. J. Milbourne: *JOM*, **23** (1971), 11.
- 3) H. Buhr and J. Pirdzun: Proc. Int. Conf. on Continuous Casting of Steel, The Metals Society and IRSID, Biarritz, (1976), 56.
- 4) L. J. Heaslip, I. D. Sommerville, A. McLean, L. Swartz and W. G. Wilson: *Iron Steelmaker*, **14** (1987), 49.
- 5) A. W. Cramb and I. Jimbo: *ISS Trans.*, **11** (1990), 67.
- 6) M. C. Tai, C. H. Chen and C. L. Chou: Proc. Continuous Casting 85, Institute of Metals, London, (1985), 19.1.
- 7) E. S. Szekeres: Proc. 4th Int. Conf. on Clean Steel, The Institute of Materials, London, (1992), 756.
- 8) I. Sasaka, T. Harada, H. Shikano and I. Tanaka: Proc. 74th Iron and Steel Society (ISS) Steelmaking Conf., Vol. 74, ISS, Warrendale, PA, (1991), 349.
- 9) L. Zhang, S. Yang, K. Cai, J. Li, X. Wan and B. G. Thomas: *Metall. Mater. Trans. B*, **38B** (2007), 63.
- 10) M. Burty, C. Pussé, M. Alvarez, P. Gaujé and G. Grehan: Proc. 84th Steelmaking Conf., ISS, Warrendale, PA, (2001), 89.
- 11) H. Bai and B. G. Thomas: *Metall. Mater. Trans. B*, **32B** (2001), 269.
- 12) Z. Liu, B. Li, M. Jiang and F. Tsukihashi: *ISIJ Int.*, **54** (2014), 1314.
- 13) T. Watanabe and M. Iguchi: *ISIJ Int.*, **49** (2009), 182.
- 14) S. Yamashita and M. Iguchi: *ISIJ Int.*, **41** (2001), 1529.
- 15) B. G. Thomas, Q. Yuan, S. Mahmood, R. Liu and R. Chaudhary: *Metall. Mater. Trans. B*, **45B** (2014), 22.
- 16) K. Jin, B. G. Thomas and X. Ruan: *Metall. Mater. Trans. B*, **47B** (2016), 548.
- 17) N. Kasai, H. Mizukami and A. Mutou: *Tetsu-to-Hagané*, **89** (2003), 1120.
- 18) Y. Miki and S. Takeuchi: *ISIJ Int.*, **43** (2003), 1548.
- 19) R. Liu and B. G. Thomas: *Metall. Mater. Trans. B*, **46B** (2015), 388.
- 20) G.-G. Lee, B. G. Thomas and S.-H. Kim: *Met. Mater. Int.*, **16** (2010), 501.
- 21) J. Klostermann, H. Chaves and R. Schwarze: *Steel Res. Int.*, **78** (2007), 595.
- 22) M. Thumfart and M. Javurek: *Steel Res. Int.*, **86** (2015), 25.
- 23) K. Timmel, N. Shevchenko, M. Roder, M. Anderhuber, P. Gardin, S. Eckert and G. Gerbeth: *Metall. Mater. Trans. B*, **43B** (2015), 700.
- 24) M. Ando: Tundish Stopper, Japanese Patent 03110048, (1991).
- 25) G. Nitzl, A. Stranimaier, H.-J. Haslinger and H. Kaufmann: Ceramic Refractory Stopper, USA Patent 2014/0217654A1, (2014).
- 26) J.-H. Lee: Stopper for Tundish Ingot Steel Exhaust Opens and Shuts, Korean Patent 10-1502023, (2015).
- 27) S. Choi, I. Lee, D. Choi, K. Choi, S. Lee and S. Sunwoo: Proc. Unified Int. Technical Conf. on Refractories (UNITECR 2013), ed. by D. G. Goski and J. D. Smith, The American Ceramic Society, Westerville, OH, (2014), 543.
- 28) H. Yasunaka, R. Yamanaka, T. Inoue and T. Saito: *Tetsu-to-Hagané*, **81** (1995), 529.
- 29) G. Abbel, W. Damen, G. D. Gendt and W. Tiekink: *ISIJ Int.*, **36** (1996), S219.
- 30) M. Wang, Y. Bao, L. Zhao, Q. Yang and L. Lin: *ISIJ Int.*, **55** (2015), 799.
- 31) H. Bai and B. G. Thomas: *Metall. Mater. Trans. B*, **32B** (2001), 1143.
- 32) P. Planquart, M. L. Riethmuller and P. Gardin: Proc. 5th European Continuous Casting Conf., The Institute of Materials, Minerals and Mining, London, (2005), 11.
- 33) N. Kasai and M. Iguchi: *Tetsu-to-Hagané*, **91** (2005), 546.
- 34) N. Kasai and M. Iguchi: *Tetsu-to-Hagané*, **91** (2005), 847.
- 35) T. Shi: M.S. thesis, University of Illinois, Urbana, IL, USA, (2001), <https://i-share.carli.illinois.edu/vf-uiu/Record/UIUdb.4479437>, (accessed 2008-09-09).
- 36) Z. Liu, L. Li, F. Qi, B. Li, M. Jiang and F. Tsukihashi: *Metall. Mater. Trans. B*, **46B** (2015), 406.
- 37) Z. Liu, F. Qi, B. Li and M. Jiang: *Metall. Mater. Trans. B*, **46B** (2015), 933.
- 38) Z. Liu, F. Qi, B. Li and S. C. P. Cheung: *Int. J. Multiph. Flow*, **79** (2016), 190.
- 39) Z. Liu, B. Li, M. Jiang and F. Tsukihashi: *ISIJ Int.*, **53** (2013), 484.
- 40) H. Mizukami, S. Hiraki and T. Watanabe: *Tetsu-to-Hagané*, **86** (2000), 152.
- 41) C. A. Schneider, W. S. Rasband and K. W. Eliceiri: *Nat. Methods*, **9** (2012), 671.
- 42) T. Young: *Philos. Trans. R. Soc. Lond.*, **95** (1805), 65.
- 43) F. M. White: Fluid Mechanics, 7th ed., McGraw-Hill, New York, (2011), 353.
- 44) R. Clift, J. R. Grace and M. E. Weber: Bubbles, Drops, and Particles, 8th Ed., Academic Press, New York, (1970), 255.
- 45) J. T. Kuo and G. B. Walis: *Int. J. Multiph. Flow*, **14** (1988), 547.
- 46) I. Leibson, E. G. Holcomb, A. G. Cacosco and J. J. Jamic: *AIChE J.*, **2** (1956), 300.
- 47) L. Davidson and E. H. Amick, Jr.: *AIChE J.*, **2** (1956), 337.
- 48) H. Ooyabu, A. Hiratsuka, R. Tsujino and M. Iguchi: *Mater. Trans.*, **50** (2009), 1812.
- 49) K. Jin, S. P. Vanka and B. G. Thomas: *Metall. Mater. Trans. B*, **49** (2018), 1360, DOI: 10.1007/s11663-018-1191-1.
- 50) T. Zhang, Z. Luo, H. Zhou, B. Ni and Z. Zou: *ISIJ Int.*, **56** (2016), 116.